Automated Method for Retinal Artery/Vein Separation via Graph Search Metaheuristic Approach

Chetan L. Srinidhi, *Student Member, IEEE*, P. Aparna, *Senior Member, IEEE*, and Jeny Rajan

***Abstract*— Separation of the vascular tree into arteries and veins is a fundamental prerequisite in the automatic diagnosis of retinal biomarkers associated with systemic and neurodegenerative diseases. In this paper, we present a novel graph search metaheuristic approach for automatic separation of arteries/veins (A/V) from color fundus images. Our method exploits local information to disentangle the complex vascular tree into multiple subtrees, and global information to label these vessel subtrees into arteries and veins. Given a binary vessel map, a graph representation of the vascular network is constructed representing the topological and spatial connectivity of the vascular structures. Based on the anatomical uniqueness at vessel crossing and branching points, the vascular tree is split into multiple subtrees containing arteries and veins. Finally, the identified vessel subtrees are labeled with A/V based on a set of hand-crafted features trained with random forest classifier. The proposed method has been tested on four different publicly available retinal datasets with an average accuracy of 94.7%, 93.2%, 96.8%, and 90.2% across AV-DRIVE, CT-DRIVE, INSPIRE-AVR, and WIDE datasets, respectively. These results demonstrate the superiority of our proposed approach in outperforming the state-of-the-art methods for A/V separation.**

***Index Terms*— Retinal image, artery/vein classification, graph search, vessel keypoints.**

I. Introduction

RETINAL microcirculation offers a unique non-invasive way to study the early manifestation of several diseases affecting the human circulatory system. Changes in retinal vascular geometrical patterns such as width, tortuosity, branching angle, junction exponents and fractal dimension have been investigated as candidate biomarkers in various ocular, systemic and neurodegenerative diseases [1]–[4]. Data from long-term population-based studies have demonstrated a consistent link between the retinal microvascular changes with incident clinical stroke [5], hypertension [6], arteriosclerosis [7], dementia [8] and other cerebral small vessel diseases [9]. For instance, the narrowing of arteries and widening of veins is a significant indicator of the progression of diabetic retinopathy (DR) [1], hypertension [7], and various other cardiovascular abnormalities [10]. Specifically, the arteriolar-to-venular diameter ratio (AVR) is a prognostic indicator of stroke, cerebral atrophy, cognitive decline and myocardial infarction [11]. Therefore, an accurate analysis and quantification of vessel specific morphological changes may provide an early insight into better understanding the pathophysiology of the disease conditions.

The retinal fundus photography is an excellent non-invasive technique most commonly used to analyse and quantify the vascular abnormalities in large-scale clinical settings, due to its speed and affordability [12]. Manual separation of artery/vein (A/V) from color fundus image is extremely time-consuming and requires an enormous amount of painstaking manual process. Hence, developing an automated tool for separation of A/V is of paramount importance in large-scale retinal disease screening programs.

Many methods have been introduced in the past for retinal A/V separation, with methods focused on either graph-based [13]–[18] or feature based techniques [19]–[28]. Among these methods, graph-based techniques rely on establishing a graph structure by uniquely representing an entire vessel tree into multiple subtrees based on utilizing the vessel connectivity information at crossing and bifurcation points. These identified vessel subtrees are further separated into A/V segments based on the pixel-wise classification of vessel centerlines. On the other hand, the feature-based techniques solely rely on pixel-level intensity information to classify vessels into A/V.

Among the feature based methods, the earliest approach for A/V separation was proposed by Grisan and Ruggeri [19]. They presented a classification technique only in a well-defined concentric zone around the optic disc region. A similar approach based on the combination of clustering and vessel tracing method was also proposed in [20]. Kondermann *et al.* [21], Niemeijer *et al.* [22] and Mirsharif *et al.* [23] explored a wide set of pixel-wise features along with different set of classifiers to obtain an

Manuscript received May 26, 2018; revised November 12, 2018 and December 11, 2018; accepted December 18, 2018. Date of publication January 1, 2019; date of current version March 21, 2019. The associate editor coordinating the review of this manuscript and approving it for publication was Dr. Yonggang Shi. *(Corresponding author: Chetan L. Srinidhi.)*

C. L. Srinidhi and P. Aparna are with the Department of Electronics and Communication Engineering, National Institute of Technology Karnataka, Surathkal 575025, India (e-mail: srinidhipy@gmail.com; p.aparnadinesh@gmail.com).

J. Rajan is with the Department of Computer Science and Engineering, National Institute of Technology Karnataka, Surathkal 575025, India (e-mail: jenyrajan@gmail.com).

This paper has supplementary downloadable material available at http://ieeexplore.ieee.org., provided by the authors. The material includes some additional results and analysis related to the work. Contact srinidhipy@gmail.com for further questions about this work.

Digital Object Identifier 10.1109/TIP.2018.2889534

optimal A/V labeling. Zamperini *et al.* [24] proposed effective feature set based on color, spatial location and vessel width, across different region-of-interest (ROI) measured from optic disc region. More recently, Welikala *et al.* [25] presented a method based on a deep neural network approach. Their approach was validated on a large population-based cohort study dataset known as UK Biobank [29]. Xu *et al.* [26] proposed first and second order textural features, along with the intensity level features to obtain a discriminative feature set for A/V separation. A novel feature extraction technique based on luminosity and reflection properties of vascular structures has been explored in Huang *et al.* [27]. A genetic search based feature selection technique for high dimensional data has been recently proposed in [28].

The significant limitations of the feature based approaches are two folds. First, due to the input image acquisition process, retinal images exhibit varying contrast and luminosity, often resulting in difficulty in distinguishing A/V segments of thin and peripheral vessels. Second, the absence of vessel connectivity information leads to difficulty in precisely tracking A/V segments of branching and crossover points. To address these issues, graph-based approaches have gained increasing interest by incorporating the structural characteristics of the retinal vascular tree. These methods exploit the distinct nature of the underlying retinal vascular connectivity pattern, that the arteries and veins will cross each other, but never with themselves [14]–[16].

Based on this assumption, several graph-theoretic approaches have been explored in the past to improve the A/V classification performance. The earliest method was proposed by Rothaus *et al.* based on a semi-automatic technique by solving a constrained graph search optimization problem [13]. Joshi *et al.* [14] presented a technique by dividing the entire vessel tree into individual subtrees, by finding an optimal path using the Dijkstra algorithm. These individual subtrees are further labeled as A/V based on a set of orientation, width, and intensity features. Dashtbozorg *et al.* [15] proposed a similar strategy by first subdividing the entire vascular tree into multiple sub-graphs based on the type of intersection points, followed by the assignment of A/V label to each vessel sub-graphs based on a set of intensity features. Estrada *et al.* [16] presented an A/V classification method for both fundus as well as scanning laser ophthalmoscope (SLO) images. They constructed a global likelihood model based on carefully designed domain-specific features to estimate the underlying vascular topology. A novel graph-based metaheuristic approach exploiting the vascular connectivity was proposed by Hu *et al.* [17]. Finally, Pellegrini *et al.* [18] proposed a novel graph cut based global optimization technique for optimal A/V separation in an ultra-wide field of view (UWFoV) SLO images, requiring no manual intervention.

Despite the considerable improvements in graph-based techniques, retinal A/V separation still suffers some difficulties. Most existing graph-based approaches mainly rely on geometrical analysis of vessel keypoints to efficiently exploit the underlying structural characteristics of a vascular network. In particular, the traditional approaches [14]–[18] utilizes only the orientation, width and intensity level information to address the challenging "*crossover issue*" encountered during a graph search process. However, one important bottleneck is that these techniques do not take into account the curvature characteristics of vascular segments, which is often critical for successful disentanglement of a highly curved crossover segment. For example, at a highly curved crossover point, the angular separation between A/V pairs will be highly skewed depending on the nature and complexity of crossing vessel segments. The vessel geometrical properties such as width, tortuosity, bifurcation/crossover angle are also prone to variations in the presence of the diseased conditions. Thus, any geometrical modelling without the inclusion of curvature information will usually produce a highly suboptimal representation of the vascular network. Further, an imperfect separation of crossing vessel pairs leads to an erroneous propagation of labels throughout the entire graph search path, resulting in inaccurate A/V separation.

In this paper, we propose a novel graph search metaheuristic approach for automatic A/V separation from retinal color fundus images. Here, we extend our previously proposed vessel keypoint detector (VKD) [30] to incorporate the curvature characteristics of crossing vessel segments, along with the orientation and width information. This curvature property acts as a unique feature to VKD to aid in resolving the possible conflict, in assigning an A/V label of the highly curved crossover point. Besides, we present a novel graph search metaheuristic algorithm to generate anatomically meaningful vessel subtrees by searching the space of possible connectivity of vascular networks.

Our main contributions can be summarized as follows:

1) We propose an extended vessel keypoint detector which integrates curvature with the orientation and width information to precisely disentangle all crossing vessel pairs into corresponding A/V segments.
2) We propose a novel depth-first search based graph search metaheuristic algorithm to accurately identify all A/V vessel subtrees from a given vascular topology.
3) We extensively validated our method on four challenging publicly available retinal datasets, including images from two different imaging modalities - fundus as well as UWFov-SLO images.

The paper is organized as follows: We first present the detail of our proposed methodology in Section II. Datasets and experimental results are described in Section III. Finally, we discuss our key findings as well as the limitations of the work in Section IV, followed by conclusions in Section V.

II. Methods

An overview of the proposed solution for automatic separation of A/V trees from retinal images is shown in Fig. 1. The pipeline consists of four main stages: identification of vessel keypoints, a graph representation of the vascular network, vessel subtree extraction and subtree A/V labeling. In the first stage, given a binary vessel map, we first identify the vessel keypoints using a vessel keypoint descriptor (VKD).

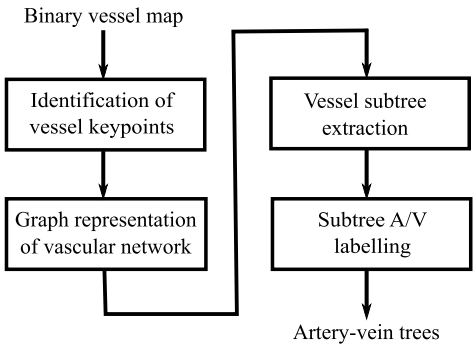

Fig. 1. An overview of the proposed A/V separation approach.

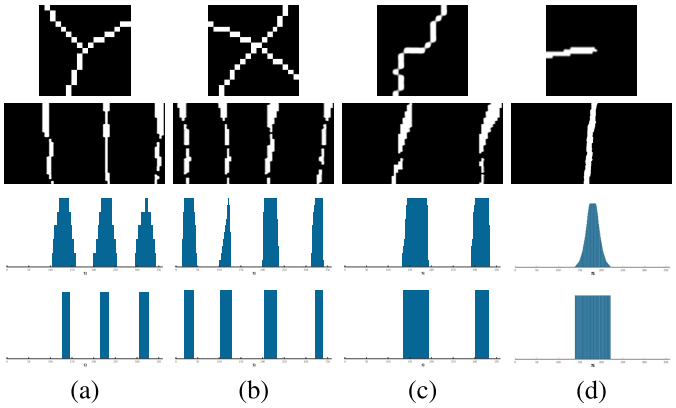

Fig. 2. Illustration of VKD. Row 1: (a) sample bifurcation; (b) crossover; (c) non-junction; and (d) a vessel endpoint patch. Row 2: the corresponding log-polar maps (with x-axis being n). Row 3: the projections of log-polar maps ($R_p(n)$). Row 4: thresholding applied to $R_p(n)$; this is the VKD descriptor.

In the second stage, the identified vessel keypoints are considered as nodes and vessel segments as edges that represents an undirected graph structure of the vascular network. In the third stage, we identify the anatomically meaningful vessel subtrees using a novel graph search metaheuristic approach by exploiting the structural connectivity of the vascular network. Finally, in the fourth stage, each vessel subtrees are given a unique A/V label based on carefully designed hand-crafted features, which are then trained using a random forest (RF) classifier.

A. Identification of Vessel Keypoints

We start by identifying vessel keypoints such as bifurcations, crossovers and vessel endpoints from a given binary vessel tree. A ROI $R_p(x, y)$ is extracted for every vessel point p in a vessel map. We eliminate the vessel centerline extraction to preserve the vessel connectivity information and to avoid errors introduced by thinning operation. A log-polar transform (LPT) is applied to the ROI to obtain $R_p(m, n)$ where, m and n are the radial and angular indices respectively. The LPT preserves information close to a vessel point while, increasingly compressing the information as one moves away from the vessel point, in a non-linear fashion. Fig. 2 (first and second row) shows the ROI for different vessel patterns of interest (branching vessels, crossing vessels, straight

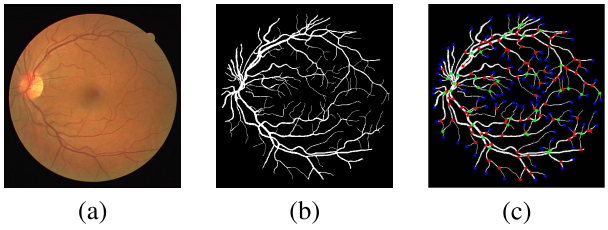

Fig. 3. (a) Original image; (b) binary vessel map; (c) identified vessel keypoints. (Note: the color red represents bifurcation point, green represents crossover point and blue represents vessel endpoints).

vessel segment and a vessel endpoint) and the corresponding log-polar mapped results. It can be observed that the number of vertical lines depend on the pattern of the vessel segment and their position depends on the orientation of vessels in $R_p(m, n)$. Where, $m \in [M_{min}, M_{max}]$; and n is the angle index, which is obtained by sampling the angular variable at 1° interval, and hence $n \in [0^\circ, 360^\circ]$. A vertical projection of $R_p(m, n)$ results in a vector $R_p(n)$, as illustrated in Fig. 2 (third row). In order to build robustness to spurious vessels and varying vessel calibre, projections at a limited set of radii (m) are considered. The obtained projection $R_p(n)$ provides a count of the number of pixels in a vessel fragment at a specific angle n. Since, only the presence or absence of vessel at a particular angle is of interest, we threshold $R_p(n)$ with $threshold = 1$ to obtain the VKD $V_p(n)$.

The VKD for four sample ROI's are shown in Fig. 2 (fourth row). Each vessel fragment gives rise to a cluster of responses in $V_p(n)$. Hence, the vessel edges are found by computing the first order difference of $V_p(n)$ as

$$V'_p(n) = \Big|V_p(n+1) - V_p(n)\Big|. \tag{1}$$

The number of vessel branches S at a point p is given as

$$S(p) = 0.5 \times \sum_n V'_p(n). \tag{2}$$

Finally, we obtain a set of keypoints $C = \{K | 1 \leq S(p) \geq 3\}$. The detected keypoints appear in the form of clusters close to junctions, which are then refined to localize the vessel keypoints. The desired candidate keypoints w are identified from cluster C by computing the entropy for every keypoint K in a 3×3 local neighbourhood, followed by non-maximum suppression within a radius of 12 pixels.

Identifying and classifying true keypoints from given w is challenging, due to the proximal presence of bifurcation and crossover points, nearby multiple junction locations, close parallel and highly curved vessels. To this end, we employ a combination of four features such as $\Big(V_w(n), R_w(n)\Big)$; basic line detector response (LD) [31]; and histogram of oriented gradients (HOG) [32], computed at every candidate keypoints w in a (17×17) neighborhood. RF classifier [33] with 500 trees is trained with these features to identify the bifurcation (b), crossover (c) and vessel end (e) points. The detected vessel keypoints for a sample image is shown in Fig. 3. These keypoints form the input to the A/V separation module, which is described next.

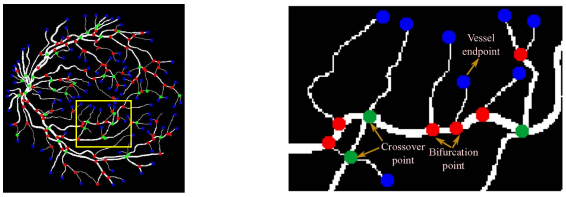

Fig. 4. (a) Graph representation of retinal vascular tree; (b) a sample ROI enlarged for visualization.

B. Graph Representation of Vascular Network

We construct a graph $\mathcal{G} = (\mathcal{V}, \mathcal{E})$, with $\mathcal{V}$ being the node and $\mathcal{E}$ being the edge of a graph. The edge $\mathcal{E}_{ij}$ represents a vessel segment that connect two nodes $(\mathcal{V}_i, \mathcal{V}_j)$ in graph $\mathcal{G}$. There exists three different types of node $\mathcal{V}$ in $\mathcal{G}$ such as:

1) Bifurcation nodes ($\mathcal{V}_b$) – correspond to vessel bifurcation points (b) (vessels of same type (A/V) bifurcates into two branches).
2) Crossover nodes ($\mathcal{V}_c$) – correspond to vessel crossover points (c) (vessels of two different types (artery-vein) crossover each other).
3) Vessel end nodes ($\mathcal{V}_e$) – correspond to vessel end points (e).

The graphical illustration of different types of node are shown in Fig. 4.

C. Vessel Subtree Extraction

In order to identify anatomically meaningful vessel trees (A/V), we divide the graph $\mathcal{G}$ into multiple subtrees $\mathcal{S}_\mathcal{G}$ using a novel graph search metaheuristic approach. The proposed graph search method is based on the two *anatomical* uniqueness of retinal vasculature:

- at *bifurcation* points, only vessels of same type bifurcate into different branches (i.e., arteries will bifurcate into arteries and same with veins).
- at *crossover* points, arteries and veins will cross each other, but never with themselves.

Based on these assumptions, we propose a two-step solution for extracting the vessel subtrees from a graph $\mathcal{G}$ as follows: (i) identification of A/V segments at a crossover location; (ii) depth-first search (DFS) based graph search approach.

1) Identification of A/V Segments at Crossover Location: A crossover point is a location where an artery crosses a vein, often leading to four vascular fragments. Out of these four, the two diagonally opposite vessel pairs belong to the same class (A/V) as shown in Fig. 5 (first and second column). In practice, there can be more than four fragments, due to branching and crossover points occurring very close to each other as shown in Fig. 5 (third and fourth column). The main bottleneck for the accurate extraction of vessel subtrees exist in identifying the appropriate A/V vessel pairs at crossover location. To this end, we model the curvature characteristics of all crossing vessel fragments, with the aid of VKD, to tackle the challenging crossover issue encountered during graph search.

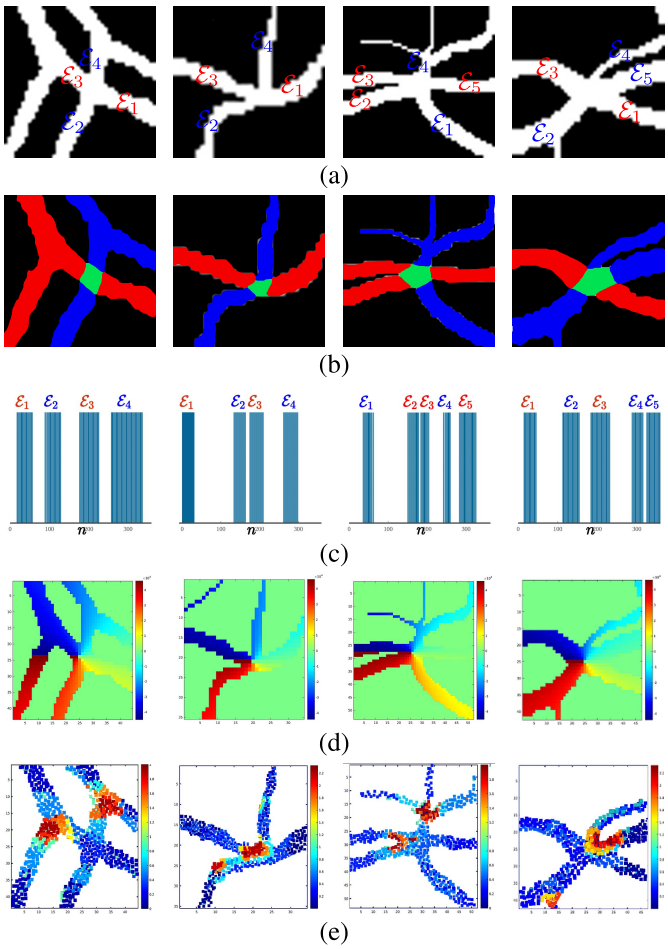

Fig. 5. (a) Binary vessel map; (b) the corresponding A/V labels (Note: the color red represents an artery, blue represents a vein and green represents a crossover point); (c) the corresponding VKD $V_p(n)$ (with x-axis being n); (d) the corresponding orientation heat-maps; (e) the corresponding curvature heat-maps. Best viewed in color.

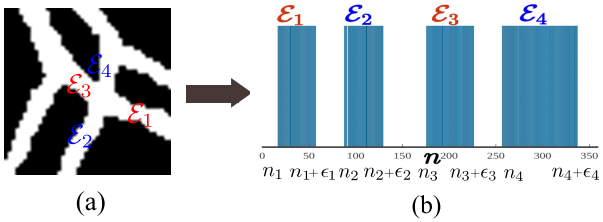

Fig. 6. Identification of corresponding pair of vascular fragments ($\mathcal{E}_i$ and $\mathcal{E}_{ip}$). (a) A sample patch with a crossover point; (b) corresponding VKD.

Given a crossover point c (see Fig. 6), the VKD(c) is given as

$$\begin{aligned}\text{VKD}(c) = &\Big[u\Big(n - n_1\Big) - u\Big(n - (n_1 + \epsilon_1)\Big)\Big] \\ &+ \Big[u\Big(n - n_2\Big) - u\Big(n - (n_2 + \epsilon_2)\Big)\Big] \\ &+ \cdots + \Big[u\Big(n - n_S\Big) - u\Big(n - (n_S + \epsilon_S)\Big)\Big] \\ = &\sum_{i=1}^{S}\Big[u\Big(n - n_i\Big) - u\Big(n - (n_i + \epsilon_i)\Big)\Big], \end{aligned} \tag{3}$$

where, $\left[u\left(n - n_i\right) - u\left(n - (n_i + \epsilon_i)\right)\right] \triangleq \mathcal{E}_i$ – refers to a specific vessel fragment ($\mathcal{E}_i$) belonging to either an artery/vein; ϵ represents the angular span of a vessel fragment; $n \in [0°, 360°]$ - assuming an angular sampling rate of 1°; and S is the number of vessel fragments converging at a crossover point, which is typically ≥ 4. Fig. 5 shows four sample artery-vein crossings (first row) and their corresponding VKDs in the third row. The first two columns represent a case of *simple* crossovers ($S = 4$ vessel fragments) and the last two columns represent a *complex* crossover case ($S > 4$ vessel fragments). The cluster of responses in VKD indicates the presence of at least one vessel fragment at a specific angle, within a window of $\geq M_{min}$. The value of M_{min} corresponds to the diameter of the largest crossing vessel segment.

From a given *crossover* point c, we make *three* important observations:

1) For every vessel fragment $\mathcal{E}_i$, there exists a vessel pair $\mathcal{E}_{ip}$ belonging to the same class (A/V), which is often separated by $n = \pm 180°$ in the VKD such that

$$\mathcal{E}_{ip} = u\Big(n - (n_i \pm 180° \pm \gamma)\Big) - u\Big(n - \big((n_i \pm 180° \pm \gamma) + \epsilon_i\big)\Big), \quad (4)$$

where, $\mathcal{E}_i$ and $\mathcal{E}_{ip}$ are vessel fragment pairs belonging to the same vessel segment (artery/vein), which are separated by an angle of $180° \pm \gamma$, as illustrated in Fig. 5 (c). γ is a small factor which accounts for highly *curved* crossover vessel segments. In Fig. 5 (first and second column), ($\mathcal{E}_1$ and $\mathcal{E}_3 = \mathcal{E}_{1p}$) or ($\mathcal{E}_2$ and $\mathcal{E}_4 = \mathcal{E}_{2p}$) are examples of ($\mathcal{E}_i$ and $\mathcal{E}_{ip}$). This is seen from the examples in Fig. 5, where the labeled fragments that are collinear are shown in red or blue (third row). This implies that a pair of vessel fragments ($\mathcal{E}_i, \mathcal{E}_{ip}$) which belongs to a single segment (A/V) are *collinear*.

2) The angular span (ϵ) of a vessel fragment which is measured with respect to c as the origin is *correlated* to its thickness. This implies a positive correlation between the width of a vessel and the corresponding cluster in VKD as shown in Fig. 5 (c). Hence for convenience, we denote the angular span (ϵ) of a vessel fragment as the vessel *width*. From Fig. 5 (a and c), it is observed that the width of the crossing vessel pairs ($\mathcal{E}_i, \mathcal{E}_{ip}$) remains almost constant, irrespective of A/V, which can be written as

$$\epsilon\{\mathcal{E}_i\} \cong \epsilon\{\mathcal{E}_{ip}\}, \quad (5)$$

where, ϵ denotes the vessel width. This is also observed to be true even for complex crossover locations as shown in Fig. 5 (third and fourth column).

3) Ideally, the vessel fragment pairs ($\mathcal{E}_i$, $\mathcal{E}_{ip}$) are given the same class label (A/V), if the angular separation of $\mathcal{E}_i \cong \mathcal{E}_{ip} \pm 180°$. But this may not always be true for high curvature crossing vessel segments as well as complex crossovers as shown in Fig. 5 (second and fourth column). The *curvature* κ is defined as "the rate of change of orientation" and determines the shape of the vessel segment. From Fig. 5 (a and e), it is observed at vessel crossings, the orientation of each vessel segment changes slightly in most cases. This implies that the rate of change of orientation for a pair of crossing vessel fragments ($\mathcal{E}_i$ and $\mathcal{E}_{ip}$) remain constant. It is also observed to be true for complex crossover locations as shown in Fig. 5 (second and fourth column). In addition, we also performed a set of experiments to detail the significance of curvature information for separation of A/V segments of different simple and challenging crossover cases, which are provided in detail in the Supplementary, Section I.

Hence, we make use of this observation to estimate the curvature (κ) of crossing vessel fragments ($\mathcal{E}_i$ and $\mathcal{E}_{ip}$) based on the following theorem.

Theorem 1: Suppose $m = R(n)$ represents a polar parametrization of a plane curve, then the curvature at any point (m, n) is given by

$$\kappa(n) = \frac{\left|R(n)^2 + 2[R'(n)]^2 - R(n)R''(n)\right|}{\{R(n)^2 + [R'(n)]^2\}^{3/2}}, \quad (6)$$

where, m and n are radial and angular indices respectively.

Proof: Let $\vec{r}(t) = (x(t), y(t))$ be a vector-valued function that traces a smooth curve α. Then the curvature (κ) of α at any point $\vec{r}(t)$ is given by (please, refer Section 1.4 of [34])

$$\kappa(t) = \frac{||\vec{r'}(t) \times \vec{r''}(t)||}{||\vec{r'}(t)||^3}. \quad (7)$$

Suppose that the curve α is given in the polar form $m = R(n)$, then curve can be parametrized as $\vec{r}(n) = (m\cos(n),\ m\sin(n),\ 0) = (R(n)\cos(n),\ R(n)\sin(n),\ 0)$. Next, we compute $\vec{r'}(n)$ by differentiating $\vec{r}(n)$ as

$$\vec{r'}(n) = -R(n)\sin(n) + R'(n)\cos(n),\ R(n).\cos(n) + R'(n)\sin(n), 0 \quad (8)$$

Similarly, we compute $\vec{r''}(n)$ by differentiating $\vec{r'}(n)$ as

$$\vec{r''}(n) = R''(n)\cos(n) - 2R'(n)\sin(n) - R(n)\cos(n), R''(n)\sin(n) + 2R'(n)\cos(n) - R(n)\sin(n), 0. \quad (9)$$

We now compute the cross product $(\vec{r'}(n) \times \vec{r''}(n))$ as

$$\begin{vmatrix} \vec{i} & \vec{j} & \vec{k} \\ -R(n)\sin(n)+R'(n)\cos(n) & R(n)\cos(n)+R'(n)\sin(n) & 0 \\ R''(n)\cos(n)-2R'(n)\sin(n) & R''(n)\sin(n)+2R'(n)\cos(n) & 0 \\ -R(n)\cos(n) & -R(n)\sin(n) & 0 \end{vmatrix} = 0,\ 0,\ 2(R'(n))^2 + (R(n))^2 - R(n). \quad (10)$$

Next, we obtain $||\vec{r'}(n) \times \vec{r''}(n)||$ as

$$\sqrt{[2(R'(n))^2 + (R(n))^2 - R(n)R''(n)]^2} = |2(R'(n))^2 + (R(n))^2 - R(n)R''(n)|. \quad (11)$$

Similarly, we compute $||\vec{r'}(n)||$ as

$$\sqrt{(R'(n))^2 + (R(n))^2} = [(R'(n))^2 + (R(n))^2]^{1/2} \quad (12)$$

Finally, we now obtain the curvature (κ) of a plane polar curve at any point (m, n) by substituting Eq. 11 and Eq. 12 in Eq. 7 as

$$\kappa(n) = \frac{\left|R(n)^2 + 2[R'(n)]^2 - R(n)R''(n)\right|}{\{R(n)^2 + [R'(n)]^2\}^{3/2}}. \quad (13)$$

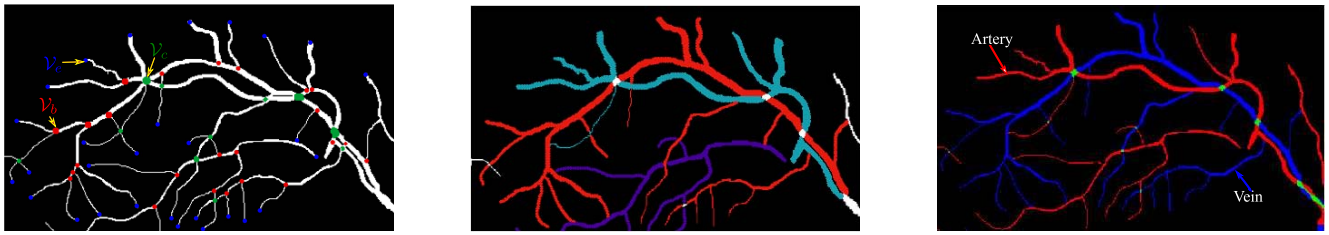

(a) (b) (c)

Fig. 7. (a) Binary vessel map (*Note:* the color red represents bifurcation nodes ($\mathcal{V}_b$), green represents crossover nodes ($\mathcal{V}_c$) and blue represents vessel end nodes ($\mathcal{V}_e$)); (b) the corresponding extracted vessel subtrees $\mathcal{S}_\mathcal{G}$, with different labels shown with different colors; (c) the corresponding subtree A/V labeling (arteries are shown in red and veins in blue).

We make use of above three observations at a crossover point to identify the corresponding pair of vascular fragments $(\mathcal{E}_i, \mathcal{E}_{ip})$ that belongs to A/V segment, as explained next.

If c is a *crossover* point, then there exists two scenarios:

1) A *simple* vessel crossover: a pair of vessels crossing each other at a point (see Fig. 5 (first and second column)). In this case, VKD is of the form

$$\text{VKD}(c) = \sum_{i=1}^{2} \Big[\mathcal{E}_i + \mathcal{E}_{ip}\Big]. \tag{14}$$

In this case, $\mathcal{E}_i$ and $\mathcal{E}_{ip}$ are given the same class label (A/V), if any of the two following *conditions* are satisfied:

a) the angular separation between two vessel pairs $(\mathcal{E}_i, \mathcal{E}_{ip})$ is often separated by $\pm 180°$:

$$\mathcal{E}_i \cong \mathcal{E}_{ip} \pm 180°; \tag{15}$$

b) the width of the crossing vessel pairs remains almost constant:

$$\epsilon\{\mathcal{E}_i\} \cong \epsilon\{\mathcal{E}_{ip}\}; \tag{16}$$

c) the curvature κ of crossing vessel pairs is relatively constant:

$$\kappa\{\mathcal{E}_i\} \approx \kappa\{\mathcal{E}_{ip}\}; \tag{17}$$

2) A *complex* vessel crossover: a pair of vessels crossing at a point and there exists a *proximal* bifurcation (see Fig. 5 (third and fourth column)). In this case, VKD is of the form

$$\text{VKD}(c) = \sum_{i=1}^{2} \Big[\mathcal{E}_i + \mathcal{E}_{ip}\Big] + \mathcal{E}_l, \tag{18}$$

where, $\mathcal{E}_l \triangleq \Big[u\Big(n - n_l\Big) - u\Big(n - (n_l + \epsilon_l)\Big)\Big]$ corresponds to a lone vessel fragment resulting from a nearby bifurcation as shown in Fig. 5 (third and fourth column). $\mathcal{E}_l$ - refers to vessel fragments $\mathcal{E}_3$ and $\mathcal{E}_4$ in third and fourth column, respectively. (*Note*: a complex crossover point generally consists of $\mathcal{E}_i > 4$ vessel fragments). Although, this is a very rare condition, we still take into account in order to build robust approach that works well irrespective of various complex crossover patterns. In this case, $\mathcal{E}_i$ and $\mathcal{E}_{ip}$ are given the same class label (A/V), if any of the two *conditions* similar to that defined for simplex crossover case are satisfied. In addition, the lone vessel fragment $\mathcal{E}_l$ is assigned a class label (A/V), if the following condition is satisfied

$$\epsilon\{\mathcal{E}_l\} \cong \epsilon\{\mathcal{E}_i\} \cong \epsilon\{\mathcal{E}_{ip}\}. \tag{19}$$

From Fig. 5 (third and forth column), $\mathcal{E}_4$ and $\mathcal{E}_3$ are the lone vessel fragments $\mathcal{E}_l$, that are assigned the same class label as $\mathcal{E}_2$ and $\mathcal{E}_5$ in third and fourth column, respectively.

Thus, given a crossover point c, VKD(c) is analysed first to identify if c represents a *simple* or *complex* case and next identify the corresponding vessel pairs of the same class (A/V) using the appropriate form of VKD.

2) Depth-First Search (DFS) Based Graph Search: To generate anatomically meaningful vessel subtrees $\mathcal{S}_\mathcal{G}$, we employ DFS based graph search algorithm to efficiently search the space of possible vascular networks. We also make use of VKD near the vessel crossover points to aid in precise labeling of all crossing segments into corresponding A/V pairs. The method of extraction of individual subtrees $\mathcal{S}_\mathcal{G}$ involves the following steps.

1) Given an undirected graph $\mathcal{G} = (\mathcal{V}, \mathcal{E})$ as shown in Fig. 7 (a), initialize the graph search using DFS at arbitrary bifurcation node $\mathcal{V}_b$, with a label l_i where, $i = 1, 2, \ldots, n$.
2) Find the neighbours associated with the node $\mathcal{V}_b$ denoted as: $\mathcal{N}_{\mathcal{V}_b}$.
3) If the associated neighbour $\mathcal{N}_{\mathcal{V}_b}$ is:
   - vessel end node ($\mathcal{V}_e$), then backtrack the DFS to $\mathcal{V}_b$.
   - vessel bifurcation node ($\mathcal{V}_b$), then continue the graph search with DFS.
   - vessel crossover node ($\mathcal{V}_c$), then set flag $\mathcal{F} = 1$ at $\mathcal{V}_c$.
4) For each crossover location c (corresponding to $\mathcal{V}_c$ at which $\mathcal{F} = 1$) proceed with the following steps:
   - first identify if c represents a *simple* or *complex* crossover point by computing VKD(c) as given in Eq. (14) and Eq. (18).
   - find the vessel fragment pair $\mathcal{E}_{ip}$ corresponding to a vessel fragment $\mathcal{E}_i$ at which $\mathcal{F} = 1$, using the conditions defined in Eq. (15), (16), (17), (19).

Algorithm 1 Subtree Generation $\mathcal{S}_{\mathcal{G}}$

Data: Binary vessel tree $\mathcal{G} = (\mathcal{V}, \mathcal{E})$

Parameters: $\mathcal{V}_b$ = vessel bifurcation nodes
$\mathcal{V}_c$ = vessel crossover nodes
$\mathcal{V}_e$ = vessel end nodes
$\mathcal{T}_{\mathcal{V}}$ = type of node $\mathcal{V}$
$\mathcal{F}$ = flag raised at crossover nodes $\mathcal{V}_c$
$\mathcal{N}_{\mathcal{V}}$ = neighbours of node $\mathcal{V}$
$\mathcal{E}_i, \mathcal{E}_{ip}$ = corresponding vessel pairs

Result: Vessel subtrees $\mathcal{S}_{\mathcal{G}}$ with labels l_i where, $i = 1, 2, .., n$

```
for i ← 1 to V do
    if T_V = V_b then
        for i ← 1 to N_{V_b} do
            start DFS at node V_b and assign a label l_i
            find N_V for node V_b
            if N_V = V_e then
                backtrack the DFS to V_b
            else if N_V = V_b then
                continue graph search with DFS
            else
                N_V = V_c; set flag F = 1 at V_c
            end
            while F = 1 do
                if c = simple crossover then
                    find the corresponding vessel pairs
                      {E_i, E_ip} as defined in Eq. (15), (16),
                      (17)
                else
                    c = complex crossover then
                    find the corresponding vessel pairs
                      {E_i, E_ip} as defined in Eq. (15), (16),
                      (17), (19)
                end
                if E_ip has already a label l_i then
                    terminate the DFS
                else
                    restart the DFS at E_ip and
                    continue the search with label l_i
                end
            end
        end
    end
end
```

- restart the graph search with DFS from the vessel fragment $\mathcal{E}_{ip}$, with the same label l_i as assigned for vessel fragment $\mathcal{E}_i$.

5) The graph search is continued until there are no more nodes $\mathcal{V}$ to visit in the current search path.
6) Search for new paths that are left unlabeled (unvisited) in the graph $\mathcal{G}$. If found, start the DFS with a new label l_i at an arbitrary bifurcation node $\mathcal{V}_b$, belonging to the new search path and continue from Step 2.
7) Continue the graph search until the entire graph $\mathcal{G}$ is labeled (as shown in Fig. 7 (b)) and no more paths to visit in the vessel tree.

The pseudocode for generating vessel subtrees $\mathcal{S}_{\mathcal{G}}$ from a graph $\mathcal{G}$ is illustrated in Algorithm 1.

There exists some misinterpretation of node labels as a result of vessel segmentation process, which affects the optimal traversal of DFS based graph search algorithm. The following are the typical errors arises during node classification: (i) bifurcation node is wrongly classified as a crossover node and vice-versa; (ii) vessel end node is wrongly classified as bifurcation node. The detailed steps to correct these node errors are provided in the Supplementary, Section V.

Each vessel subtree $\mathcal{S}_{\mathcal{G}}$ corresponds to different labels l_i, where $i = 1, 2, .., n$ as shown in Fig. 7 (b) (*Note:* the subtrees generated doesn't imply A/V segments at this stage, and each vessel subtree is independent of the other having different labels l_i). Hence, to obtain the optimal A/V labels for the entire graph $\mathcal{G}$, each vessel subtree is given a unique label (A/V) based on a set of hand-crafted features extracted from vessel pixels corresponding to each vessel subtree, as described next.

TABLE I
LIST OF FEATURES EXTRACTED FOR A/V CLASSIFICATION

Index	Feature description
1-9	Vessel pixel intensity in Red, Green, Blue Hue, Saturation, Brightness and Lab color space.
10-45	Mean, standard deviation, minimum and maximum intensities of Red, Green, Blue, Hue, Saturation, Brightness and Lab vessel maps.
46-55	Vessel centerline pixel intensity in a Gaussian blurred ($\sigma = 2, 4, 8, 12, 16$) of Red and Green Channel.
56	Vessel width* (ϵ) calculated at the centerline pixel location of the binary vessel map.
57-66	Vessel cross-sectional intensity profile† in Red and Green channel.

* The vessel width (ϵ as defined in Eq. 5) of a segment is measured with respect to centerline pixel as the origin.
† The vessel profile was determined using VKD with respect to every centerline pixels, within a ROI of [$M_{min} = 3$ pixels, $M_{max} = 7$ pixels].

D. Subtree A/V Labeling

For the identified vessel subtrees, the final goal is to assign an A/V label based on a set of hand-crafted features extracted from the vessel pixels, corresponding to each vessel subtree $\mathcal{S}_{\mathcal{G}}$. Since retinal images often exhibit varying contrast and luminosity, we pre-process each input image using the method proposed in [35]. A set of 66-D hand-crafted feature vector (as shown in Table I) is extracted for every vessel pixel, and further normalized to zero mean and unit standard deviation. Some of these features were adopted in [11], [15], and [19] and have shown to be robust for A/V separation. The vessel width and cross-sectional intensity features are detailed in Appendix A and Appendix B, respectively. These features were trained using RF classifier of 200 trees to predict the A/V label of each vessel subtree $\mathcal{S}_{\mathcal{G}}$. A thorough discussion on the performance comparison of different classifiers and feature selection techniques are also provided in Section IV-B.

A vessel subtree $\mathcal{S}_{\mathcal{G}}$ is assigned with a label artery (A), if the majority of the vessel pixels associated with a subtree are classified as arteries; else if the majority of the pixels are classified

as veins, it is labeled with a vein (V). Further, to prevent the erroneous A/V separation as result of graph search analysis, we also calculate the probability of individual vessel segment (belonging to a vessel subtree) being an A/V, without considering the result of graph search approach. A vessel segment is assigned a label artery (A), if the probability of being an artery $P_A \geq 0.9$ (90% of the pixels are being classified as arteries); else if the probability of being a vein $P_V \geq 0.9$, it is assigned with a label vein (V). A thorough performance analysis of A/V separation without and with segment-wise analysis is provided in the Supplementary, Section II. A subtree A/V labeling for a sample ROI is shown in Fig. 7 (c) with color red representing arteries and blue representing veins.

III. Experimental Results

A. Materials

For validating the effectiveness of proposed method, we tested on four different publicly available datasets: AV-DRIVE [36], CT-DRIVE [15], INSPIRE-AVR [11] and WIDE [16]. The AV-DRIVE consists of 40 images (565×584 pixels) derived from earlier DRIVE dataset [37], with ground truth (GT) A/V labels marked for all vessel pixels. Since three different human graders manually classified all the vessel pixels, a majority consensus was taken to arrive at the final A/V labeling. The CT-DRIVE consists of 20 images corresponding to the DRIVE test set [37] with A/V labels graded only for vessel centerline pixels. The INSPIRE-AVR consists of 40 images (2392×2048 pixels) with associated A/V labels obtained from [15] for vessel centerline pixels, only. Finally, the WIDE dataset provides 30 SLO-images (3900×3072 pixels) along with their A/V GT labels obtained from [16].

The input binary vessel map for all four datasets was obtained automatically from the raw color image using the method proposed in [38]. Since, CT-DRIVE, INSPIRE-AVR, and WIDE dataset consists of manual A/V markings for centerline pixels, we subsequently thinned the binary vessel map to obtain vessel centerlines [39]. The obtained centerline maps usually consist of various misinterpretation of vascular structures as a result of thinning operation, which was further corrected using the technique proposed in [15]. This refinement aimed at resolving critical issues such as missing vessel segment, splitting of crossover into two nearby bifurcations and the deletion of a false vessel segment.

B. Evaluation Metrics

The performance validation was carried out using three metrics: *Sensitivity* (Se), *Specificity* (Sp) and *Accuracy* (Acc).

$$Se = \frac{TP}{TP + FN}, \quad Sp = \frac{TN}{TN + FP}, \quad Acc = \frac{TP + TN}{N},$$

where, TP/FP denotes true/false positives; TN/FN denotes true/false negatives; and the total $N = TP + TN + FN + FP$. In our method, we consider arteries as positives and veins as negatives. Accordingly, sensitivity is defined as how well the method can detect arteries, while specificity indicates how well it can detect veins.

TABLE II
Comparative Analysis of the Proposed Methods on AV-DRIVE Dataset

Method	Accuracy	Sensitivity	Specificity	Time (sec)
Estrada *et al.* [16]	0.935	0.930	**0.941**	131.32
Xu *et al.* [26]	0.923	0.915	0.929	**5.00**
Welikala *et al.* [25]	0.912	–	–	–
Hu *et al.* [17]	0.880	–	–	–
Huang *et al.* [28]	0.720	0.709	0.738	
DFS-search	0.896	0.918	0.875	124.70
RF-only	0.746	0.779	0.713	36.40
DFS-search + RF	**0.947**	**0.966**	0.929	161.10

C. A/V Separation Evaluation

In the following subsections, we present the results of our proposed A/V separation method on each of the four retinal datasets. We validated the approach at each stage of the pipeline starting from vessel subtree extraction to the final A/V labeling of the entire vascular network.

The method "*DFS-search*" refers to the output at vessel subtree extraction stage, where we manually assign A/V labels for individual vessel subtrees. The "*RF-only*" refers to the classification of vessel pixels into A/V by using hand-crafted features (shown in Table I) trained with RF classifier (without considering any graph-search analysis). Finally, "*DFS-search with RF"* refers to our method's final output after subtree A/V labeling stage, which uses combined knowledge of graph-search analysis and RF classifier for predicting the final A/V label of the entire vessel tree.

1) AV-DRIVE Dataset: The AV-DRIVE consists of pre-partitioned training and test set, each of which contains 20 images. The sample A/V separation results on DRIVE images are shown in Fig. 8. It is observed that the proposed method accurately classifies most of the A/V segments in the DRIVE set, including the region of thin and low contrast vessels. Most of the false classifications are due to the presence of nearby junction points and missing vessel connectivity, especially around the optic disc area. A similar ambiguity has also been observed with expert human graders in assigning A/V labels in and around the optic disc, which further showcase the difficulty of this A/V separation problem.

Table II shows the performance of the proposed approach with state-of-the-art methods on the AV-DRIVE dataset. Our proposed method has shown a significant improvement in Se of 0.966, with a relatively high Sp of 0.929, clearly indicating that the system is capable of identifying arteries than the veins. This is also shown to be consistent with Fig. 8, where a majority of the wrongly classified vessel pixels belongs to the veins (shown in green).

2) CT-DRIVE Dataset: A leave-one-out cross-validation was adopted for evaluation of 20 images of the CT-DRIVE dataset. Classification of vessel pixels which are higher than 3 pixels wide is considered for performance assessment [15]. The sample A/V separation results on the CT-DRIVE dataset

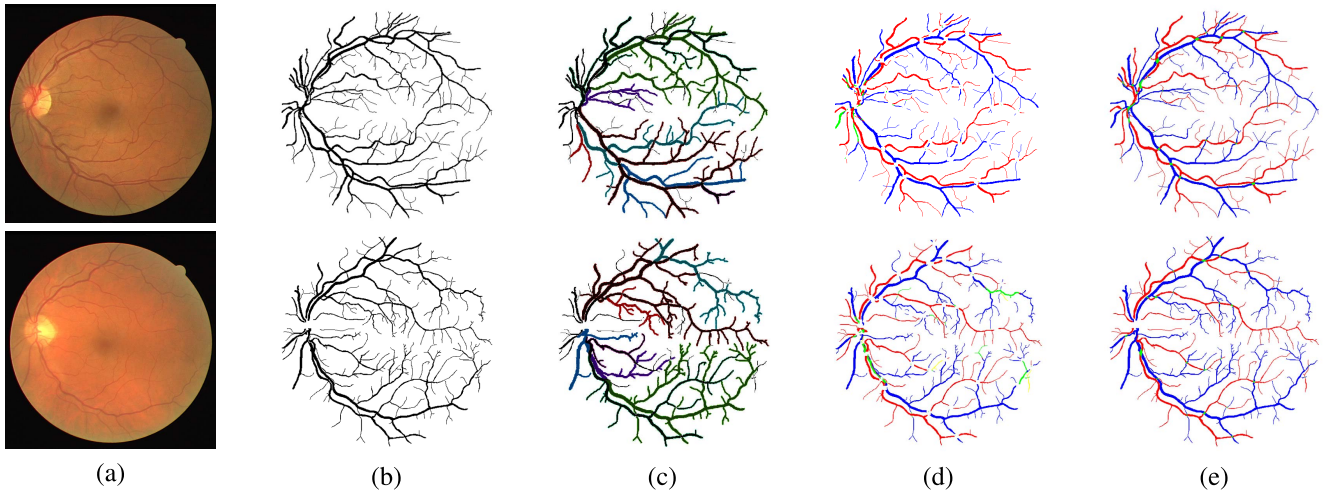

Fig. 8. AV-DRIVE separation results. Top row: our method's best result ($Acc = 0.985$). Bottom row: our method's worst result ($Acc = 0.889$). (a) Original image; (b) binary vessel map; (c) identified vessel subtrees; (d) A/V separation results; (e) corresponding A/V ground truth. (*Note*: the correctly labeled arteries/veins are shown in red/blue, respectively. While, incorrectly labeled arteries/veins are shown in yellow/green, respectively). Best viewed in color.

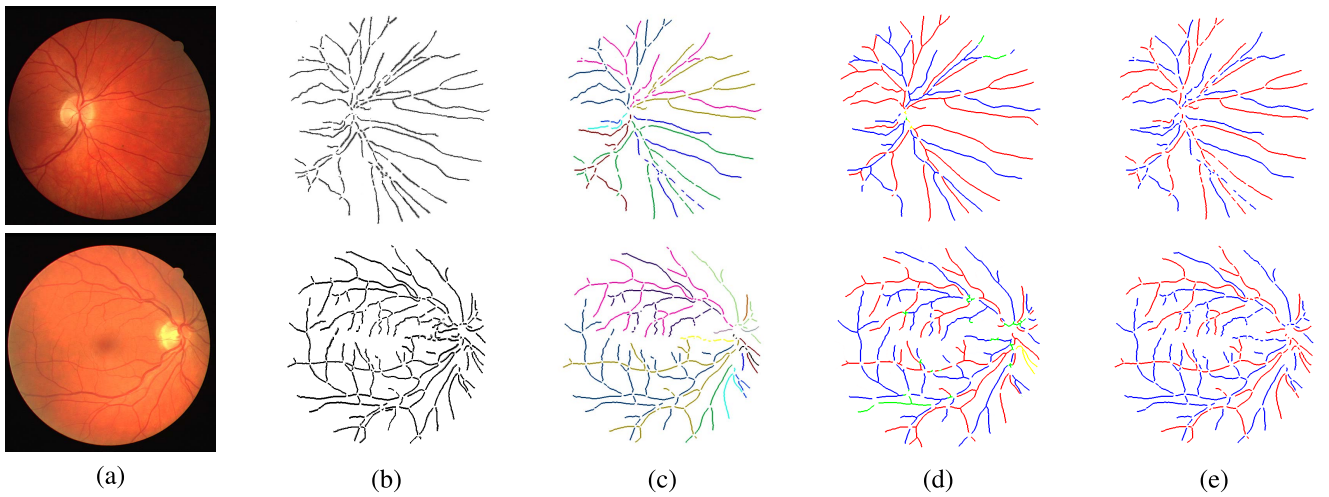

Fig. 9. CT-DRIVE separation results. Top row: our method's best result ($Acc = 0.981$). Bottom row: our method's worst result ($Acc = 0.864$). (a) Original image; (b) binary vessel map; (c) identified vessel subtrees; (d) A/V separation results; (e) corresponding A/V ground truth. (*Note*: the correctly labeled arteries/veins are shown in red/blue, respectively. While, incorrectly labeled arteries/veins are shown in yellow/green, respectively). Best viewed in color.

is shown in Fig. 9. Our method achieved a very high *Se* of 0.950, which is $\approx$ 3% greater than previous approaches on the same dataset, as shown in Table III. Similar to the AV-DRIVE dataset, much of the false positives are in the optic disc region. The thinning of closely spaced junction structures especially in the optic disc region, often resemble spurious and isolated fragments, leading to difficulty in obtaining any meaningful information about the vessel morphology. Henceforth, a marginal decrease in A/V performance is observed on CT-DRIVE dataset compared to AV-DRIVE, as shown in Table III. A similar trend has also been observed with earlier methods [11], [15], that depends on centreline map as an input to their approach.

TABLE III

COMPARATIVE ANALYSIS OF THE PROPOSED METHODS ON CT-DRIVE DATASET

Method	Accuracy	Sensitivity	Specificity	Time (sec)
Estrada *et al.* [16]	0.917	0.917	**0.917**	**131.32**
Dashtbozorg *et al.* [15]	0.874	0.900	0.840	–
Niemeijer *et al.* [11]	N/A	0.800	0.800	–
DFS-search	0.909	0.924	0.895	109.00
RF-only	0.753	0.781	0.726	34.00
DFS-search + RF	**0.932**	**0.950**	0.915	143.00

3) INSPIRE-AVR Dataset: For the evaluation of A/V separation on INSPIRE-AVR dataset, we adopted a 2-fold cross-validation. In this approach, we divide the dataset into two random equal sized partitions, each containing 20 images. One partition is used as train set while, the other partition as test set and vice-versa. Examples of A/V separation on INSPIRE-AVR dataset is shown in Fig. 10. Table IV shows

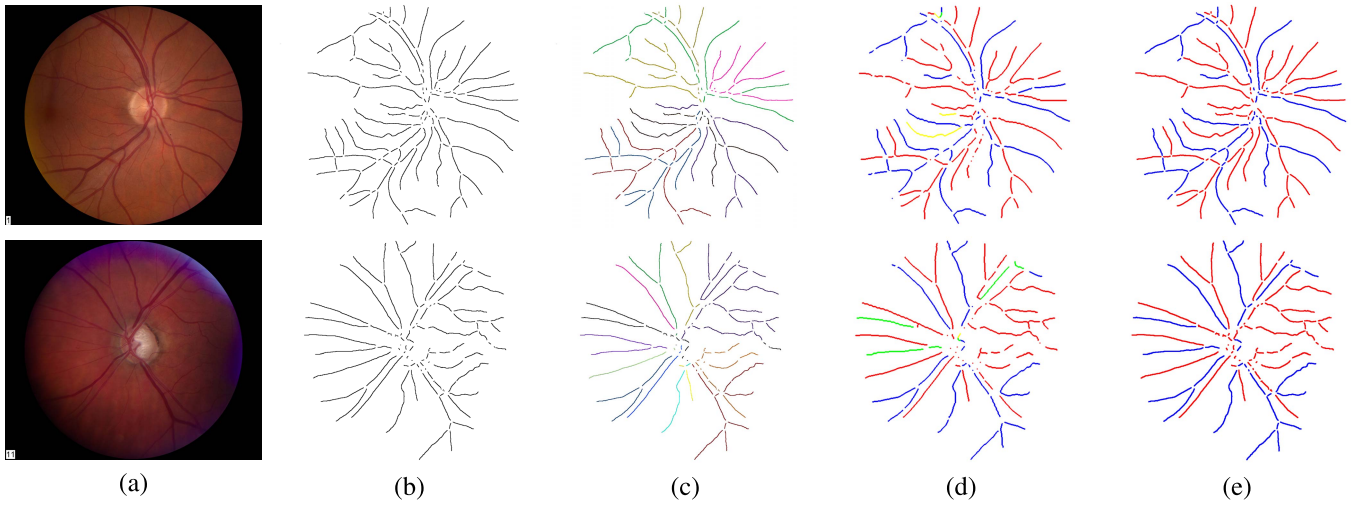

Fig. 10. INSPIRE-AVR separation results. Top row: our method's best result ($Acc = 0.989$). Bottom row: our method's worst result ($Acc = 0.926$). (a) Original image; (b) binary vessel map; (c) identified vessel subtrees; (d) A/V separation results; (e) corresponding A/V ground truth. (*Note*: the correctly labeled arteries/veins are shown in red/blue, respectively. While, incorrectly labeled arteries/veins are shown in yellow/green, respectively). Best viewed in color.

TABLE IV
COMPARATIVE ANALYSIS OF THE PROPOSED METHODS ON INSPIRE-AVR DATASET

Method	Accuracy	Sensitivity	Specificity	Time (sec)
Estrada *et al.* [16]	0.909	0.915	0.902	117.68
Dashtbozorg *et al.* [15]	0.849	0.910	0.860	–
Niemeijer *et al.* [11]	N/A	0.780	0.780	–
Huang *et al.* [27]	0.851	N/A	N/A	–
DFS-search	0.921	0.945	0.897	62.13
RF-only	0.682	0.691	0.674	14.95
DFS-search + RF	**0.968**	**0.969**	**0.966**	**77.08**

TABLE V
COMPARATIVE ANALYSIS OF THE PROPOSED METHODS ON WIDE DATASET

Method	Accuracy	Sensitivity	Specificity	Time (sec)
Estrada *et al.* [16]	**0.910**	0.910	**0.909**	777.35
Pellegrini *et al.* [18]	0.862	N/A	N/A	–
DFS-search	0.861	0.891	0.831	209.40
RF-only	0.741	0.763	0.719	54.58
DFS-search + RF	0.902	**0.923**	0.882	**263.98**

the comparative analysis of the proposed approach with state-of-the-art methods. We obtain an Acc value of 0.968 and Se of 0.969, which is 5% higher than the most recent results reported in Estrada *et al.* [16]. The INSPIRE-AVR dataset contains only fewer vessel structures and complex junction locations, which subsequently resulted in better A/V separation compared to AV/CT-DRIVE datasets.

We also further evaluated the proposed method by considering only six major A/V vessels within a region of 1-DD to 1.5-DD, as this ROI was normally used for AVR calculation [11]. We obtain a Acc value of 0.991, which is $1\%(Acc = 0.971)/15\%(Acc = 0.84)$ greater than previously reported methods [11], [15], respectively. For the sake of fair comparison, we obtain a Se value of 0.981 from the ROC curve, for a fixed Sp of 0.860 reported in [11] and [15]. Thus, the proposed approach is also shown to be reliable in developing an automated solution for quantifying AVR in retinal images.

4) WIDE Dataset: In the WIDE dataset, a 2-fold cross-validation approach is adopted by randomly assigning images into two sets, each containing 15 images. The sample A/V results of the WIDE dataset is shown in Fig. 11. When compared with other three datasets, A/V separation on the WIDE dataset is most challenging because of very low-contrast noisy images. These artefacts are more prominent in the peripheral regions containing thin and low contrast vessel structures as shown in Fig. 11. Besides, the number of extracted vessel subtrees are significantly large due to the wider FOV followed by relatively lower spatial resolution, which is a typical case in SLO modality. Nevertheless, the proposed method was able to achieve a better Acc/Se value of 0.902/0.923, which is comparatively higher than the most recent method proposed in Pellegrini *et al.* [18], as shown in Table V. Many of the false detections are mainly observed in the proximal region of multiple junction locations, thin and very low-contrast vessel areas (see Fig. 11). The extracted vessel subtrees are also found to be suboptimal in these locations mainly because of the presence of erroneous vessel structures formed during vessel thinning operation. Furthermore, the pixel-wise features extracted from these regions were also found to be less discriminative, often leading to many false classifications.

IV. DISCUSSION

The proposed method consists of series of interlinked stages, where the performance of each stage depends on its previous

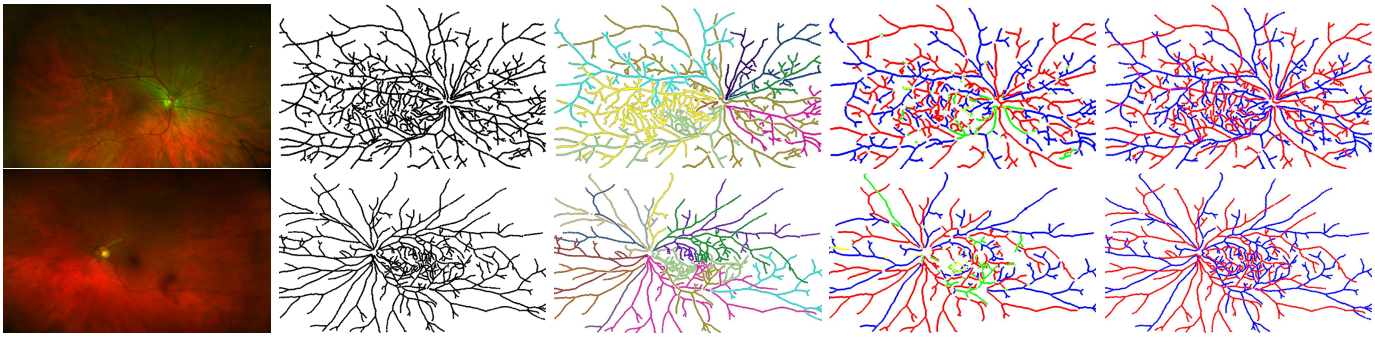

(a) (b) (c) (d) (e)

Fig. 11. WIDE separation results. Top row: our method's best result ($Acc = 0.939$). Bottom row: our method's worst result ($Acc = 0.827$). (a) Original image; (b) binary vessel map; (c) identified vessel subtrees; (d) A/V separation results; (e) corresponding A/V ground truth. (*Note*: the correctly labeled arteries/veins are shown in red/blue, respectively. While, incorrectly labeled arteries/veins are shown in yellow/green, respectively). Best viewed in color.

stage output. Hence, to validate the robustness of our approach, we evaluate the performance at each stage starting from: (i) identification of vessel subtrees - which is referred to as "DFS-search"; (ii) A/V classification using only hand-crafted features - which is referred to as "RF-only"; and (iii) finally, subtree A/V labeling stage (which combines both the knowledge of graph search and hand-crafted features) - which is referred to as "DFS-search with RF". We also further investigate the relative importance of hand-crafted features using different feature selection techniques as well as various classifiers to examine the impact on final A/V labeling.

A. Performance Analysis of Each Stage Output

The proposed three-stage refinement steps accurately predicts the A/V labeling from four different datasets, including images from fundus as well as SLO image modalities. In Section II, it was shown how each of these steps contributes to yield a more accurate solution progressively. The experimental analysis also confirms this view, where it has been empirically shown, how each stage output improves upon the previous stage.

We first evaluate the A/V separation at the output of DFS-search by manually assigning A/V labels for individual vessel subtrees. We obtain an average $Acc > 86\%$ across all four datasets (see Table II - Table V), while depending solely on the knowledge of graph search. This underscores the richness of metaheuristic approach - which efficiently exploits local as well as global vessel connectivity information to precisely track all the A/V segments from a given vascular network. A highest Acc of 0.921 is observed on INSPIRE-AVR dataset, while the lowest Acc of 0.861 is on the WIDE dataset. This is because the INSPIRE-AVR dataset consists of a fewer number of graph linking structures - including the number of complex crossovers when compared to the WIDE dataset.

We also observed a substantial improvement in mean Acc of 15% (AV-DRIVE), 15.6% (CT-DRIVE), 23.9% (INSPIRE-AVR) and 12% (WIDE), when compared with DFS-search to the RF-only stage. The pixel level intensity-based features have shown to be vulnerable to varying image conditions such as resolution, contrast and illumination artefacts both within and across datasets. Finally, the combination of DFS-search with RF have shown a modest improvement in the Acc value of 5.1% (AV-DRIVE), 2.3% (CT-DRIVE), 4.7% (INSPIRE-AVR) and 4.1% (WIDE) from DFS-search to DFS-search with RF stage. This consistent improvement strongly indicates that the system is more accurate while relying on more complex knowledge of vessel connectivity as well as pixel-level feature information for classifying A/V.

TABLE VI

PERFORMANCE COMPARISON (Acc) OF DIFFERENT COMBINATION OF CLASSIFIERS AND FEATURE SELECTION TECHNIQUES ON AV-DRIVE/INSPIRE-AVR DATASETS

Classifier/ Feature selection	NB	LDA	k-NN	SVM	RF
None	0.909/ 0.945	0.921/ 0.923	0.875/ 0.938	0.886/ 0.902	**0.947/ 0.968**
SFS	0.914/ 0.938	0.908/ 0.924	0.893/ 0.918	0.898/ 0.902	0.923/ 0.954
Lasso	0.926/ 0.906	0.897/ 0.892	0.862/ 0.873	0.887/ 0.884	0.909/ 0.927
ENet	0.897/ 0.910	0.885/ 0.903	0.871/ 0.891	0.869/ 0.876	0.916/ 0.935

* The acronym stands for 'SFS' - Sequential Forward Selection; 'LASSO' - Least Absolute Shrinkage and Selection Operator; 'ENet' - Elastic Net; 'NB' - Naive Bayes; 'LDA' - Linear Discriminant Analysis; 'k-NN - k-Nearest Neighbor; 'SVM' - Linear Support Vector Machine; and 'RF' - Random Forest classifiers.

B. Influence of Feature Selection vs. Classifiers

In this section, we investigate the relative significance of hand-crafted features using a combination of various feature selection techniques with different classifiers. The experimental results on AV-DRIVE and INSPIRE-AVR datasets are reported in Table VI with same dataset split as mentioned in Section III-C1 and Section III-C3, respectively.

To evaluate the importance of features on classification accuracy, we adopted a combination of feature selection techniques such as sequential forward selection, LASSO [40], and ENet [41], with different classifiers such as Naive Bayes, LDA, k-NN, SVM, and RF. The RF classifier with no feature selection proved to be the most reliable combination with a

Acc of 0.947/0.968 across AV-DRIVE and INSPIRE-AVR, respectively. This indicates that all the selected features given in Table I have a strong influence on final A/V labeling and have shown discriminative ability, even with varying imaging conditions such as contrast and luminosity. Further, the selected feature set captures both intensity (raw pixel intensities in RGB, HSI and Lab color space) as well as structural level information (such as vessel width) that aid in accurate separation of arteries from veins. Compared to different classifiers, RF has shown better performance due to its ability to perform both classification and feature selection implicitly.

C. Computation Time

The proposed automated A/V separation method was developed in MATLAB R2017 (MathWorks, Inc.), with an average computation time of 4.3 minutes per image (across all four datasets) using an Intel Core i7-5960 CPU at 3.00 GHz. We also reported the running time at each stage of the A/V separation pipeline that is shown in Table II - Table V. The DFS-based graph search is the most computationally intensive stage, which can be further improved by utilizing parallel processing capabilities (as discussed in Supplementary, Section VI) and through more efficient implementation.

V. Conclusion

In this paper, we have presented a comprehensive graph search metaheuristic approach for separating arteries from veins in retinal images. The proposed method formulates the A/V separation as a graph search problem by incorporating sophisticated graph-theoretic knowledge with the domain-specific priors, to accurately identify A/V segments across the entire vascular tree. In this work, we explore the vessel curvature criteria in addition to orientation and width information, to precisely disseminate the A/V label information of highly curved crossovers, encountered during graph search process. Such limitation was not addressed previously in many state-of-the-art methods [14]–[18] that utilizes graph theoretic knowledge, unlike the proposed approach. The inclusion of hybrid knowledge of both local and global vessel connectivity during graph traversal often helps in identifying anatomically meaningful vessel subtrees by searching the space of possible vascular networks. The proposed method was validated on four different challenging datasets including images from the narrow field (AV-DRIVE, CT-DRIVE, and INSPIRE-AVR datasets) and wide field-of-view (WIDE dataset) fundus photographs, with remarkable differences in resolution, quality, and acquisition protocol. Overall, there is a significant improvement in A/V separation performance across the entire range of diversity and might enable real-time analysis in the future.

Appendix A
Vessel Width Calculation

The vessel width (ϵ) of a segment is measured using VKD [30] for every centerline pixels of the binary vessel map, as illustrated in Fig. 12. Let us consider a point $p(x, y)$ on a centerline map to which a log-polar transform is applied to obtain $p(m, n)$. Where, m and n are the radial and angular indices, respectively. The value $'m'$ is empirically chosen as 8 pixels, so that it covers the width of the widest vessels in all four datasets (AV-DRIVE, CT-DRIVE, INSPIRE-AVR, and WIDE), and must be fixed only once during training. Further, the angle index n is obtained by sampling the angular variable at every 1° interval, and hence $n \in [0°, 360°]$.

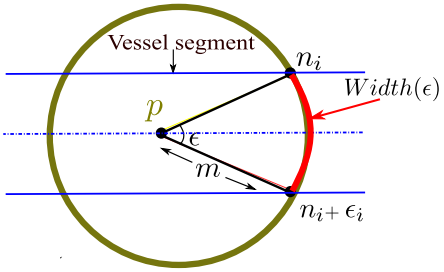

Fig. 12. Vessel width estimation for a sample vessel segment. p is a point on the centerline pixel location (x, y) of the binary vessel map. ϵ is the angular span between vessel intersection points $(n_i, n_i + \epsilon_i)$, which is referred to as *vessel width*; and m is the radial distance.

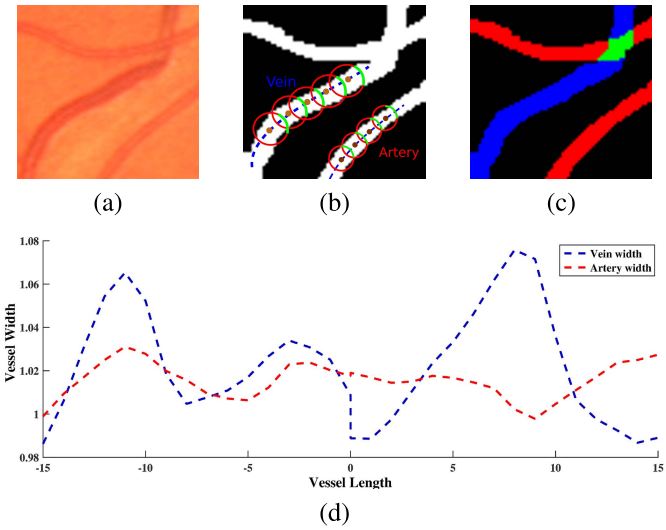

Fig. 13. A sample vessel width estimation for artery-vein segments. (a) Original image patch; (b) the corresponding binary vessel map illustrating the width estimation for a sample artery and vein segments; (c) the corresponding A/V ground truth; (d) artery and vein vessel width (shown in red and blue, respectively) calculated for a sample of 30 centerline pixels, as shown in (b); *Note:* the y-axis corresponds to the normalised width values, obtained by dividing with its mean width corresponding to the entire vessel length.

We now denote the angular span of the vessel segment at a radial distance m as the *vessel width* (ϵ), with the end points of vessel $(n_i, n_i + \epsilon_i)$ subtending an angle ϵ at point p, as shown in Fig. 12. The sample vessel width measurements for artery-vein segments are shown in Fig. 13 (d). Note that, the width of the vein segment is relatively larger than an artery, which is an important feature in distinguishing artery-vein segments. Also note that in Fig. 13 (d), the y-axis corresponds to the normalised width values, obtained by dividing with its mean width corresponding to the entire vessel length.

Appendix B
Vessel Profile Estimation

The vessel profile was determined using VKD [30] for every centerline pixels in red and green channel image. We describe

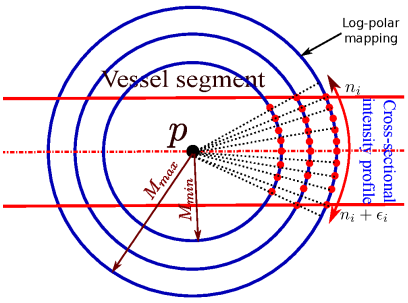

Fig. 14. Vessel cross-sectional intensity profile for a sample vessel segment. p is a point on the centerline pixel location (x, y) of the red/green channel image. M_{min} and M_{max} are the inner and outer most radii, respectively. The angular orientations: $n \in [n_i,\ n_i + \epsilon_i]$ (*red dots*), along with which the vessel intensity profile is estimated for artery-vein segments.

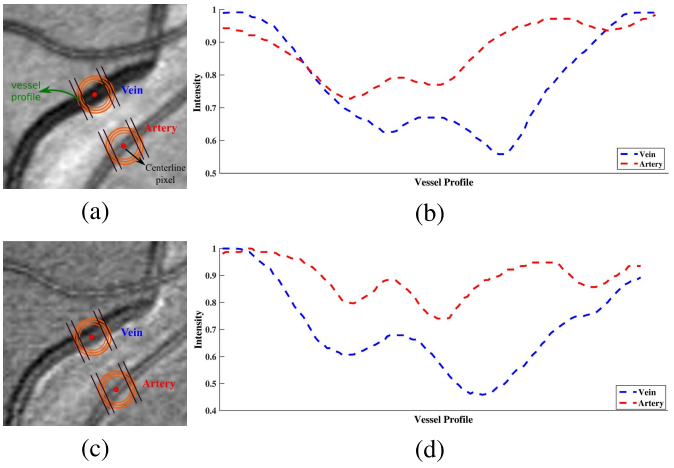

Fig. 15. (a) A sample retinal image patch (shown in *green* channel), with its corresponding vessel intensity profiles on the artery and vein are shown in (b); (c) a sample retinal image patch (shown in *red* channel), with its corresponding vessel intensity profiles on the artery and vein are shown in (d). *Note:* the intensity values in y-axis are normalized between 0 and 1; x-axis corresponds to vessel profile in the angular range $(n_i, n_i + \epsilon_i)$ sub-sampled at 10 equally spaced angular locations.

this briefly as follows: first an ROI $R_p(x, y)$ is extracted for every centerline pixels $p(x, y)$ in the red and green channel map. A log-polar transform is applied to the ROI to obtain $R_p(m, n)$ as illustrated in Fig. 14. Where, $m \in [M_{min}, M_{max}]$ is the radial index; and n is the angle index, which is obtained by sampling the angular variable at 1° interval, and hence $n \in [0°, 360°]$.

Next, we compute a vertical projection of $R_p(m, n)$ which results in a vector $R_p(n)$. The $R_p(n)$ provides a count of the number of pixels in a vessel fragment at specific angle n. Further, we limit the ROI $R_p(n)$ to a range $n \in [n_i, n_i + \epsilon_i]$ to estimate the cross-sectional intensity profile as shown in Fig. 14 (the red dots). A mean vessel intensity value is computed at every specific angle n (along the projection), which is then sub-sampled at 10 equally spaced angular locations between $(n_i, n_i + \epsilon_i)$ to obtain the final cross-sectional intensity feature $(I_p(n))$. The value $M_{min} = 3$ pixels and $M_{max} = 7$ pixels are chosen experimentally, according to the vessel widths (both wide and small vessels) of all four retinal datasets (AV-DRIVE, CT-DRIVE, INSPIRE-AVR, and WIDE). Fig. 15 (b) and Fig. 15 (d) shows the sample cross-sectional vessel intensity profile in green and red channel image, respectively.

ACKNOWLEDGEMENT

The authors would like to thank Touseef Qureshi for providing AV-Drive images, Behdad Dashtbozorg for providing CT-DRIVE images, Meindert Niemeijer for providing INSPIRE-AVR images and Rolando Estrada for providing WIDE images. They would also like to gratefully thank the anonymous reviewers for their insightful comments and constructive feedback, which immensely helped in improving the quality of this manuscript.

REFERENCES

[1] M. D. Abramoff, M. K. Garvin, and M. Sonka, "Retinal imaging and image analysis," *IEEE Rev. Biomed. Eng.*, vol. 3, pp. 169–208, 2010.
[2] C. Y.-L. Cheung, M. K. Ikram, C. Chen, and T. Y. Wong, "Imaging retina to study dementia and stroke," *Prog. Retinal Eye Res.*, vol. 57, pp. 89–107, Mar. 2017.
[3] S. M. Heringa, W. H. Bouvy, E. van den Berg, A. C. Moll, L. J. Kappelle, and G. J. Biessels, "Associations between retinal microvascular changes and dementia, cognitive functioning, and brain imaging abnormalities: A systematic review," *J. Cerebral Blood Flow Metabolism*, vol. 33, no. 7, pp. 983–995, Jul. 2013.
[4] S. McGrory *et al.*, "The application of retinal fundus camera imaging in dementia: A systematic review," *Alzheimer's Dementia Diagnosis, Assessment Disease Monitor.*, vol. 6, pp. 91–107, Dec. 2016.
[5] T. Y. Wong *et al.*, "Retinal microvascular abnormalities and incident stroke: The atherosclerosis risk in communities study," *Lancet*, vol. 358, no. 9288, pp. 1134–1140, Oct. 2001.
[6] C. Y.-L. Cheung, M. K. Ikram, C. Sabanayagam, and T. Y. Wong, "Retinal microvasculature as a model to study the manifestations of hypertension," *Hypertension*, vol. 60, no. 5, pp. 1094–1103, Nov. 2012.
[7] L. D. Hubbard *et al.*, "Methods for evaluation of retinal microvascular abnormalities associated with hypertension/sclerosis in the atherosclerosis risk in communities study," *Ophthalmology*, vol. 106, no. 12, pp. 2269–2280, Dec. 1999.
[8] S. Frost *et al.*, "Retinal vascular biomarkers for early detection and monitoring of Alzheimer's disease," *Transl. Psychiatry*, vol. 3, no. 2, p. e233, Feb. 2013.
[9] T. Y. Wong *et al.*, "Cerebral white matter lesions, retinopathy, and incident clinical stroke," *Proc. JAMA*, vol. 288, no. 1, pp. 67–74, 2002.
[10] T. Y. Wong *et al.*, "Quantitative retinal venular caliber and risk of cardiovascular disease in older persons: The cardiovascular health study," *Arch. Int. Med.*, vol. 166, no. 21, pp. 2388–2394, Nov. 2006.
[11] M. Niemeijer *et al.*, "Automated measurement of the arteriolar-to-venular width ratio in digital color fundus photographs," *IEEE Trans. Med. Imag.*, vol. 30, no. 11, pp. 1941–1950, Nov. 2011.
[12] C. L. Srinidhi, P. Aparna, and J. Rajan, "Recent advancements in retinal vessel segmentation," *J. Med. Syst.*, vol. 41, no. 4, p. 70, Apr. 2017.
[13] K. Rothaus, X. Jiang, and P. Rhiem, "Separation of the retinal vascular graph in arteries and veins based upon structural knowledge," *Image Vis. Comput.*, vol. 27, no. 7, pp. 864–875, Jun. 2009.
[14] V. S. Joshi, J. M. Reinhardt, M. K. Garvin, and M. D. Abramoff, "Automated method for identification and artery-venous classification of vessel trees in retinal vessel networks," *PLoS ONE*, vol. 9, no. 2, p. e88061, Feb. 2014.
[15] B. Dashtbozorg, A. M. Mendonça, and A. Campilho, "An automatic graph-based approach for artery/vein classification in retinal images," *IEEE Trans. Image Process.*, vol. 23, no. 3, pp. 1073–1083, Mar. 2014.
[16] R. Estrada, M. J. Allingham, P. S. Mettu, S. W. Cousins, C. Tomasi, and S. Farsiu, "Retinal artery-vein classification via topology estimation," *IEEE Trans. Med. Imag.*, vol. 34, no. 12, pp. 2518–2534, Dec. 2015.
[17] Q. Hu, M. D. Abràmoff, and M. K. Garvin, "Automated construction of arterial and venous trees in retinal images," *J. Med. Imag.*, vol. 2, no. 4, p. 044001, Oct. 2015.
[18] E. Pellegrini, G. Robertson, T. MacGillivray, J. van Hemert, G. Houston, and E. Trucco, "A graph cut approach to artery/vein classification in ultra-widefield scanning laser ophthalmoscopy," *IEEE Trans. Med. Imag.*, vol. 37, no. 2, pp. 516–526, Feb. 2018.

[19] E. Grisan and A. Ruggeri, "A divide et impera strategy for automatic classification of retinal vessels into arteries and veins," in *Proc. 25th Annu. Int. Conf. IEEE Eng. Med. Biol. Soc.*, vol. 1, Sep. 2003, pp. 890–893.

[20] S. G. Vazquez, B. Cancela, N. Barreira, M. G. Penedo, and M. Saez, "On the automatic computation of the arterio-venous ratio in retinal images: Using minimal paths for the artery/vein classification," in *Proc. Int. Conf. Digital Image Comput. Techn. Appl.*, Dec. 2010, pp. 599–604.

[21] M. Yan, C. Kondermann, and D. Kondermann, "Blood vessel classification into arteries and veins in retinal images," *Proc. SPIE*, vol. 6512, p. 651247, Mar. 2007.

[22] M. Niemeijer, B. van Ginneken, and M. D. Abrámoff, "Automatic classification of retinal vessels into arteries and veins," *Proc. SPIE*, vol. 7260, p. 72601F, Feb. 2009.

[23] Q. Mirsharif, F. Tajeripour, and H. Pourreza, "Automated characterization of blood vessels as arteries and veins in retinal images," *Computerized Med. Imag. Graph.*, vol. 37, nos. 7–8, pp. 607–617, Oct./Dec. 2013.

[24] A. Zamperini, A. Giachetti, E. Trucco, and K. S. Chin, "Effective features for artery-vein classification in digital fundus images," in *Proc. 25th IEEE Int. Symp. Comput.-Based Med. Syst. (CBMS)*, Jun. 2012, pp. 1–6.

[25] R. Welikala *et al.*, "Automated arteriole and venule classification using deep learning for retinal images from the UK biobank cohort," *Comput. Biol. Med.*, vol. 90, pp. 23–32, Nov. 2017.

[26] X. Xu, W. Ding, M. D. Abrámoff, and R. Cao, "An improved arteriovenous classification method for the early diagnostics of various diseases in retinal image," *Comput. Methods Programs Biomed.*, vol. 141, pp. 3–9, Apr. 2017.

[27] F. Huang, B. Dashtbozorg, and B. M. ter Haar Romeny, "Artery/vein classification using reflection features in retina fundus images," *Mach. Vis. Appl.*, vol. 29, no. 1, pp. 23–34, Jan. 2018.

[28] F. Huang, B. Dashtbozorg, T. Tan, and B. M. ter Haar Romeny, "Retinal artery/vein classification using genetic-search feature selection," *Comput. Methods Programs Biomed.*, vol. 161, pp. 197–207, Jul. 2018.

[29] (2017). *UK Biobank*. [Online]. Available: http://www.ukbiobankeyeconsortium.org.uk

[30] C. L. Srinidhi, P. Rath, and J. Sivaswamy, "A vessel keypoint detector for junction classification," in *Proc. 14th Int. Symp. Biomed. Imag.*, Apr. 2017, pp. 882–885.

[31] E. Ricci and R. Perfetti, "Retinal blood vessel segmentation using line operators and support vector classification," *IEEE Trans. Med. Imag.*, vol. 26, no. 10, pp. 1357–1365, Oct. 2007.

[32] N. Dalal and B. Triggs, "Histograms of oriented gradients for human detection," in *Proc. IEEE Comput. Soc. Conf. Comput. Vis. Pattern Recognit.*, vol. 1, Jun. 2005, pp. 886–893.

[33] L. Breiman, "Random forests," *Mach. Learn.*, vol. 45, no. 1, pp. 5–32, 2001.

[34] E. Abbena, S. Salaman, and A. Gray, *Modern Differential Geometry of Curves and Surfaces with Mathematica*, 1st ed. Boca Raton, FL, USA: CRC Press, 1996.

[35] M. Foracchia, E. Grisan, and A. Ruggeri, "Luminosity and contrast normalization in retinal images," *Med. Image Anal.*, vol. 9, no. 3, pp. 179–190, Jun. 2005.

[36] T. A. Qureshi, M. Habib, A. Hunter, and B. Al-Diri, "A manually-labeled, artery/vein classified benchmark for the DRIVE dataset," in *Proc. 26th IEEE Int. Symp. Comput.-Based Med. Syst.*, Jun. 2013, pp. 485–488.

[37] J. Staal, M. D. Abramoff, M. Niemeijer, M. A. Viergever, and B. van Ginneken, "Ridge-based vessel segmentation in color images of the retina," *IEEE Trans. Med. Imag.*, vol. 23, no. 4, pp. 501–509, Apr. 2004.

[38] G. Azzopardi, N. Strisciuglio, M. Vento, and N. Petkov, "Trainable COSFIRE filters for vessel delineation with application to retinal images," *Med. Image Anal.*, vol. 19, no. 1, pp. 46–57, Jan. 2015.

[39] T. Y. Zhang and C. Y. Suen, "A fast parallel algorithm for thinning digital patterns," *Commun. ACM*, vol. 27, no. 3, pp. 236–239, Mar. 1984.

[40] R. Tibshirani, "Regression shrinkage and selection via the lasso," *J. Roy. Stat. Soc. Ser. B, Methodol.*, vol. 58, no. 1, pp. 267–288, 1996.

[41] H. Zou and T. Hastie, "Regularization and variable selection via the elastic net," *J. Roy. Stat. Soc. Ser. B, Methodol.*, vol. 67, no. 2, pp. 301–320, 2005.

Authors' photograph and biography not available at the time of publication.